Report

Neuron

Posterior Neocortex-Specific Regulation of Neuronal Migration by CEP85L Identifies Maternal Centriole-Dependent Activation of CDK5

Highlights

- Mutations in *CEP85L* cause posterior-specific pachygyria
- CEP85L is required for neuronal migration
- Loss of *CEP85L* disrupts centrosome organization and function
- CEP85L localizes and activates CDK5 at the centrosome

Authors

Andrew Kodani, Connor Kenny, Abbe Lai, ..., David G. Vossler, Christopher J. Yuskaitis, Christopher A. Walsh

Correspondence

andrew.kodani@childrens.harvard.edu (A.K.), christopher.walsh@childrens.harvard.edu (C.A.W.)

In Brief

Neuronal migration is essential for brain architecture during neurodevelopment. Kodani et al. demonstrate that the pachygyria gene *CEP85L* is required to organize the centrosome and microtubule cytoskeleton to promote coordinated neuronal migration by activating the neuronal kinase CDK5 at the centrosome.

Kodani et al., 2020, Neuron *106*, 1–10
April 22, 2020
https://doi.org/10.1016/j.neuron.2020.01.030

CellPress

Please cite this article in press as: Kodani et al., Posterior Neocortex-Specific Regulation of Neuronal Migration by CEP85L Identifies Maternal Centriole-Dependent Activation of CDK5, Neuron (2020), https://doi.org/10.1016/j.neuron.2020.01.030

Neuron
Report

Posterior Neocortex-Specific Regulation of Neuronal Migration by CEP85L Identifies Maternal Centriole-Dependent Activation of CDK5

Andrew Kodani,[1,2,*] Connor Kenny,[1,2,17] Abbe Lai,[1,2,3,17] Dilenny M. Gonzalez,[1,2] Edward Stronge,[1,2] Gabrielle M. Sejourne,[1,2] Laura Isacco,[1,2] Jennifer N. Partlow,[1,2] Anne O'Donnell,[1,2,4] Kirsty McWalter,[5] Alicia B. Byrne,[4,6,7] A. James Barkovich,[8] Edward Yang,[9] R. Sean Hill,[1,2] Pawel Gawlinski,[10] Wojciech Wiszniewski,[10,11] Julie S. Cohen,[12,13] S. Ali Fatemi,[12,13,14] Kristin W. Baranano,[12,13] Mustafa Sahin,[3] David G. Vossler,[15] Christopher J. Yuskaitis,[3,16] and Christopher A. Walsh[1,2,18,*]

[1]Division of Genetics and Genomics and Howard Hughes Medical Institute, Boston Children's Hospital, Boston, MA, USA
[2]Department of Pediatrics and Neurology, Harvard Medical School, Boston, MA, USA
[3]Department of Neurology, Boston Children's Hospital, Boston, MA, USA
[4]Center for Mendelian Genomics, The Broad Institute of MIT and Harvard, Cambridge, MA, USA
[5]GeneDX, Gaithersburg, MD, USA
[6]Department of Genetics and Molecular Pathology, Centre for Cancer Biology, SA Pathology, Adelaide, SA, Australia
[7]School of Pharmacy and Medical Sciences, University of South Australia, Adelaide, SA, Australia
[8]Department of Radiology, University of California, San Francisco, San Francisco, CA, USA
[9]Department of Radiology, Boston Children's Hospital, Boston, MA, USA
[10]Department of Medical Genetics, Institute of Mother and Child, Warsaw, Poland
[11]Department of Molecular and Medical Genetics, Oregon Health and Science University, Portland, OR, USA
[12]Division of Neurogenetics, Kennedy Krieger Institute, Baltimore, MD, USA
[13]Department of Neurology, Johns Hopkins University School of Medicine, Baltimore, MD, USA
[14]Department of Pediatrics, Johns Hopkins University School of Medicine, Baltimore, MD, USA
[15]Department of Neurology, University of Washington, Seattle, WA, USA
[16]Division of Epilepsy and Neurophysiology, Department of Neurology, Boston Children's Hospital, Boston, MA, USA
[17]These authors contributed equally
[18]Lead Contact
*Correspondence: andrew.kodani@childrens.harvard.edu (A.K.), christopher.walsh@childrens.harvard.edu (C.A.W.)
https://doi.org/10.1016/j.neuron.2020.01.030

SUMMARY

Genes mutated in human neuronal migration disorders encode tubulin proteins and a variety of tubulin-binding and -regulating proteins, but it is very poorly understood how these proteins function together to coordinate migration. Additionally, the way in which regional differences in neocortical migration are controlled is completely unknown. Here we describe a new syndrome with remarkably region-specific effects on neuronal migration in the posterior cortex, reflecting *de novo* variants in *CEP85L*. We show that CEP85L is required cell autonomously *in vivo* and *in vitro* for migration, that it localizes to the maternal centriole, and that it forms a complex with many other proteins required for migration, including CDK5, LIS1, NDE1, KIF2A, and DYNC1H1. Loss of CEP85L disrupts CDK5 localization and activation, leading to centrosome disorganization and disrupted microtubule cytoskeleton organization. Together, our findings suggest that CEP85L highlights a complex that controls CDK5 activity to promote neuronal migration.

INTRODUCTION

Orderly migration of neurons from the ventricular zone to the developing cerebral cortex is critical for laminar organization of the cortex (Rakic, 1971), and disruption of neuronal migration underlies the pathogenesis of lissencephaly (LIS), a disorder characterized by a reduction in cortical brain folds, with patients exhibiting a range of cognitive and motor defects (Di Donato et al., 2017). More than a dozen genes for neuronal migration disorders have been identified, with many of them encoding centrosomal proteins required for microtubule cytoskeleton organization (Di Donato et al., 2018), but many cases still remain unexplained. Moreover, how the LIS-associated proteins interact and organize at the centrosome is largely unknown. Here we describe a strikingly novel condition reflecting mutations in *CEP85L* that causes posteriorly restricted pachygyria (reduced, coarse cerebral cortical folds) because of disrupted centrosome and microtubule cytoskeleton organization, and we show that CEP85L represents a critical organizational link between many other centrosomal LIS-associated proteins.

RESULTS

De Novo Variants in *CEP85L* Cause Posterior-Specific Pachygyria

Whole-exome sequencing and targeted sequencing of a cohort of families with variable pachygyria identified seven individuals

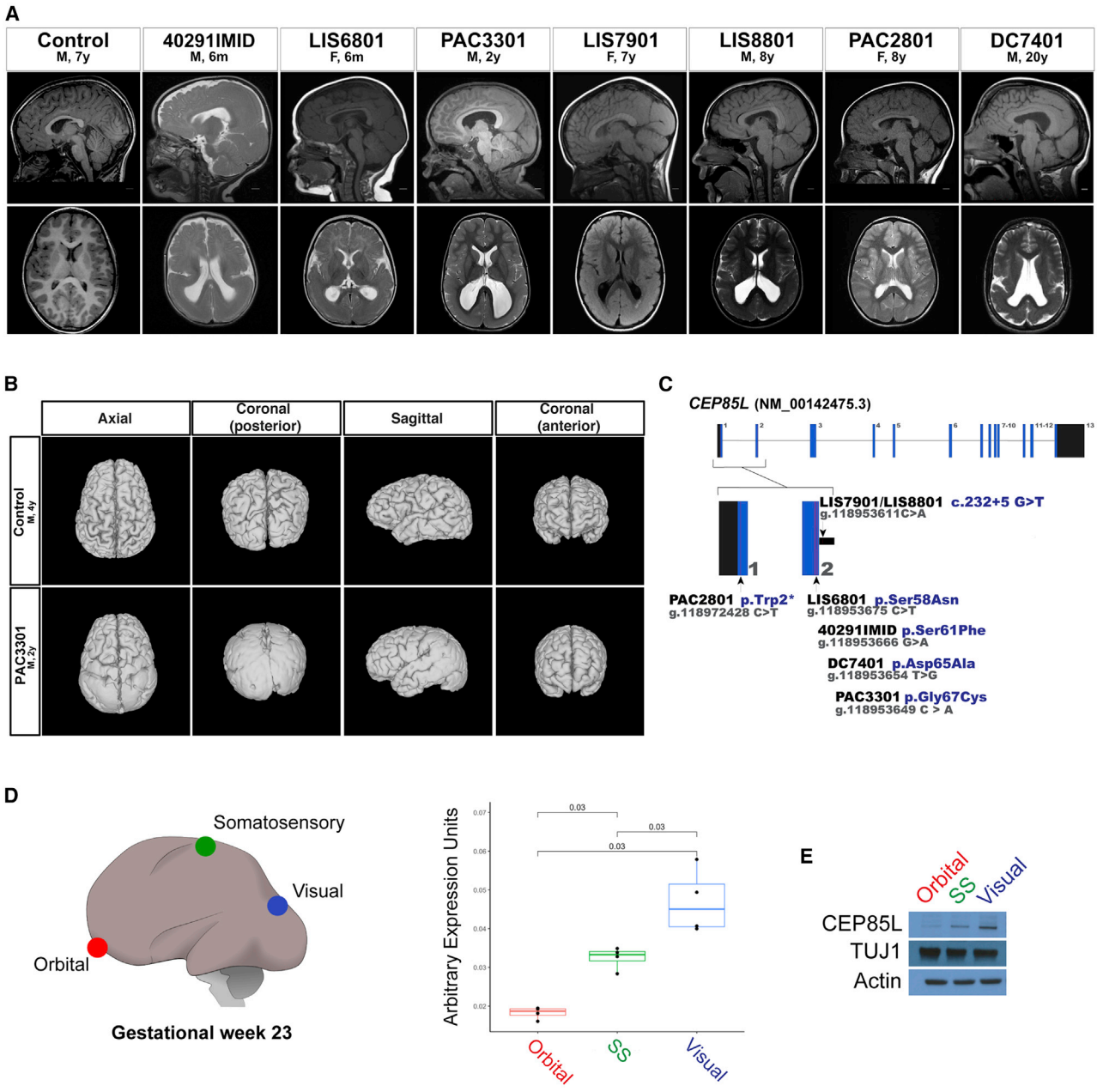

Figure 1. Variants in *CEP85L* Cause Posterior-Specific Pachygyria

(A) Sagittal and axial plane MRI images of control and affected individuals with posterior reduced gyral folding.

(B) 3D MRI presentation of a control and PAC3301 patient with a *de novo CEP85L* variant.

(C) Schematic representation of exons of *CEP85L* (blue bars). The variants in *CEP85L* are found in exons 1 and 2.

(D) Brain region-specific qPCR of gestational week (GW) 23 cortex, demonstrating the increasing rostral-to-caudal expression pattern of CEP85L normalized to β-actin. Shown is the orbital (red), somatosensory (green), and visual (blue) cortex. For quantification, one brain region was analyzed in triplicate or quadruplicate ($n = 1$). $p < 0.03$ (Student's t test).

(E) Whole-cell lysate from the posterior frontal, parietal, and occipital lobes of a GW23 fetus blotted for CEP85L and the LIS-associated protein LIS1. Actin and TUJ1 served as a loading control and neuron-specific sampling control, respectively.

with variants in the *CEP85L* gene with a strikingly similar radiographic and clinical phenotype (Figure 1A; Table S1). The cortical malformation in all cases included bilateral posterior-predominant pachygyria consisting of a thin cortex, a thin cell-sparse zone underlying the cortex, and a thickened subcortical band, involving the parietal, occipital, and temporal lobes but completely sparing the cortex rostral to the central sulcus (Figure 1B; Videos S1 and S2). All seven affected individuals had

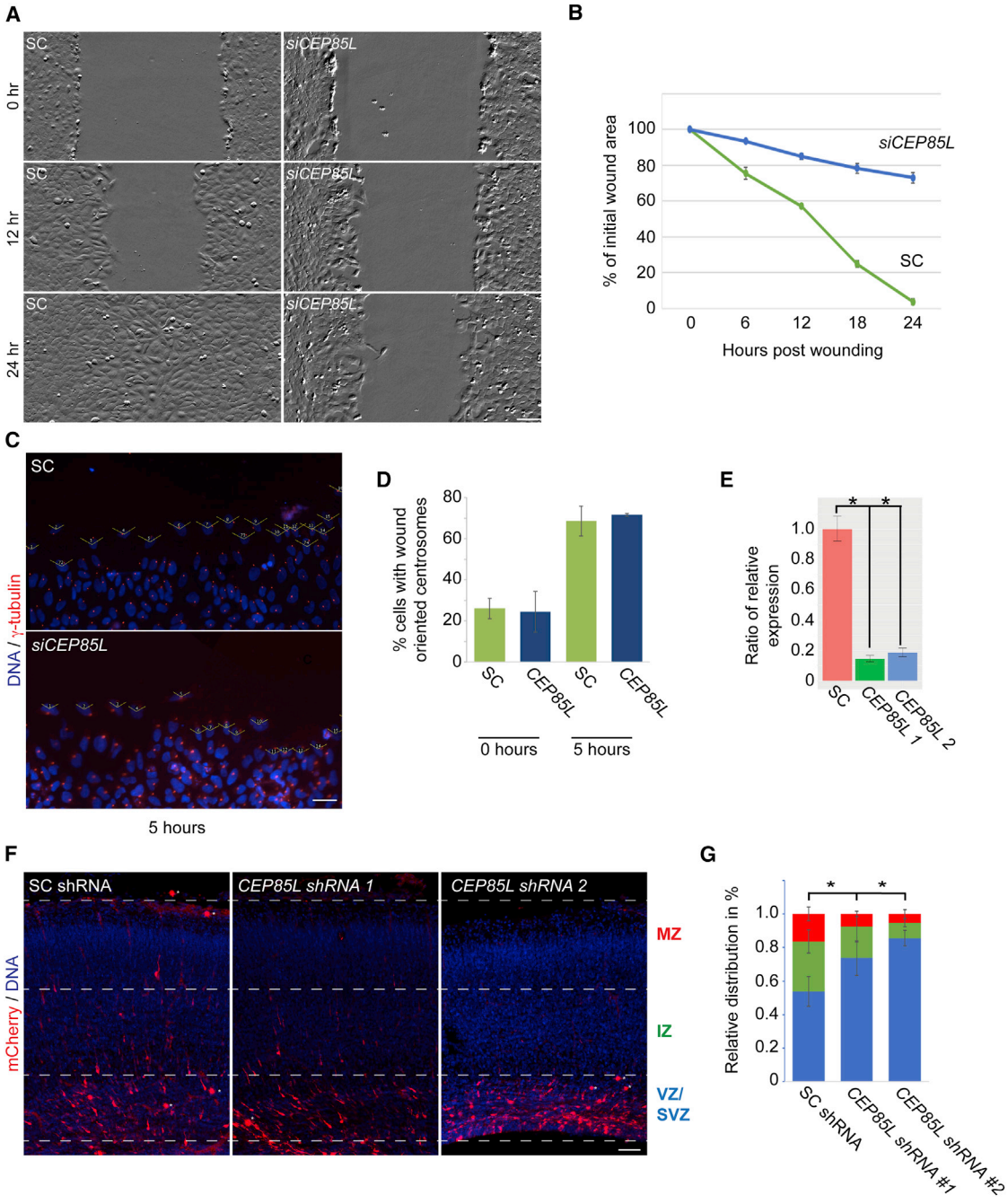

Figure 2. CEP85L Is Required for Neuronal Migration

(A) Time-lapse stills from scratch wound assays of scrambled control (SC) and *CEP85L* siRNA-transfected U2-OS cells. Confluent monolayers were wounded using a P200 tip and imaged over 24 h using a Zeiss Celldiscoverer 7.

(B) Quantifications of the areas of migration at the indicated time points of SC and *CEP85L*-depleted cells. For all quantifications, three distinct experiments were performed.

(C) Immunostaining of γ-tubulin (red) and DNA (blue) in SC and *CEP85L* siRNA-transfected cells along the wound edge. Open-faced triangles are facing the wound. The scale bar represents 200 μm for all images.

(D) Percentage of cells along the wound edge with centrosomes oriented toward the wound at 0 and 5 h. For all quantifications, 100 cells were analyzed per experiment (n = 3). $p < 0.005$ (Student's t test).

(E) qRT-PCR of SC and *Cep85l #1* and *Cep85l #2* shRNA-transfected cells normalized to β-actin and represented as a ratio of the control.

(legend continued on next page)

decreased white matter and a dysmorphic corpus callosum. Two of the individuals also exhibited Chiari I malformations. All exhibited developmental delay or intellectual disability but had learned to walk. Affected individuals suffered from seizures, either focal or epileptic spasms. Despite the dramatic posterior malformation, cortical visual impairment was not noted. Four individuals exhibited strabismus (three had esotropia, and one had exotropia), and one individual had convergence insufficiency. All individuals had head circumferences in the normal range and did not display consistent dysmorphic facial features.

We initially identified three subjects (PAC2801, DC7401, and LIS6801) from whole-exome sequencing (WES) of 36 unrelated families with LIS, pachygyria, or subcortical-band heterotopia who lacked pathogenic variants in known LIS genes (n = 3 of 36). Two additional variants (LIS8801 and PAC3301) were identified by targeted sequencing of *CEP85L* in 11 individuals with posterior predominant LIS. WES of LIS8801 and PAC3301 was performed to rule out other disease-causing variants. The two remaining individuals with *CEP85L* variants were identified using GeneMatcher and had been discovered by trio exome sequencing (40291IMID and LIS7901).

Four individuals carry missense variants in exon 2 of *CEP85L*, and three of these were confirmed to be *de novo* (c.182C > T, p.Ser61Phe; c.194A > C, p.Asp65Ala; c.199G > T, p.Gly67Cys). Parental samples were unavailable for LIS6801 (c.173G > A, p.Ser58Asn). PAC2801 has a *de novo* nonsense variant in exon 1 (c.5G > A, p.Trp2Ter), whereas two unrelated individuals, LIS7901 and LIS8801, both share the same recurrent variant in the splice donor site of exon 2 (c.232+5 G > T) that is predicted to result in skipping of exon 2 (Figure 1C; Table S2). The variant in LIS7901 was confirmed to be *de novo*, but both parental samples were unavailable for LIS8801. All variants were verified by Sanger sequencing and were absent from normals in the 1000 Genomes and gnomAD databases. To test the enrichment of *de novo CEP85L* mutations in gyral disorders, we compared the frequency of *CEP85L* mutations in our cohort of 36 exome-sequenced LIS cases (3 of 36) to 43,502 trios with various diagnoses sequenced at GeneDX, where 6 *de novo CEP85L* variants were found (6 of 43,502), demonstrating highly significant enrichment of *de novo CEP85L* mutations in patients with gyral abnormalities ($p < 6 \times 10^{-8}$, Fisher's exact test).

In the developing human and mouse, NM_00142475.3 is the major isoform expressed in the fetal brain (Johnson et al., 2015; de Rie et al., 2017). Ensemble and Refseq denote a second isoform of CEP85L, NM_001178035, which differs from the NM_00142475.3 transcript in its alternative start codon and 5′ UTR. The variants reported here all affect the NM_00142475.3 transcript. Although CEP85L is not severely constrained for missense or loss-of-function (LoF) variants, with many LoF changes in gnomAD, the two exons carrying the variants reported here show greater constraint than other exons (>95.9%) (Havrilla et al., 2019), and all disease-associated missense variants were clustered within 10 amino acids, suggesting that the first two exons are essential for CEP85L function.

The posterior-predominant malformation suggests that *CEP85L* expression is higher in the posterior cortex during development; this was confirmed by quantitative PCR (qPCR) of samples from the orbital frontal, somatosensory, and visual cortex of human gestational week (GW) 23 brain (Figure 1D). CEP85L protein levels were also higher in the visual relative to the orbital cortex, whereas TUJ1, a marker shared by all neurons, was more uniform (Lee et al., 1990; Figure 1E). The posterior-predominant malformation is similar to, but much sharper, than that seen with mutations in *LIS1* (Guerrini et al., 2000) and *DYNC1H1* (Jamuar et al., 2014). Although *LIS1* levels were uniform across brain regions (Figure 1E), the similarity nonetheless suggested potentially close functional interactions of CEP85L with LIS1 and DYNC1H1.

CEP85L Is Required for Neuronal Migration

A scratch wound healing assay suggested that CEP85L is required cell autonomously for migration. U2-OS cells transfected with small interfering RNA (siRNA) directed against *CEP85L* or scrambled control (SC) demonstrated (Figure 2A; Videos S3 and S4) that control cells filled the wounded area over 24 h, whereas *CEP85L*-depleted cells failed to migrate into the wound (Figure 2B). SC and *CEP85L* siRNA-transfected cells could properly orient their centrosomes toward the wound, which is the first step in the wound response, suggesting that the failure of migration is not due to defective cell polarization (Figures 2C and 2D).

Knockdown of *Cep85l* in mice using short hairpin RNA (shRNA) demonstrated a cell-autonomous requirement in migrating cortical neurons. We confirmed the efficiency of the *Cep85l* shRNA constructs by transfecting mouse Neuro-2a cells with the SC or two nonoverlapping *Cep85l* shRNA constructs, observing that both targeting constructs suppressed mRNA levels in more than 90% of controls (Figure 2E). We next examined whether CEP85L regulates cortical migration by electroporating an mCherry construct along with SC or *Cep85l* shRNA into embryonic day 14.5 wild-type mice. Electroporated brains analyzed 3 days after electroporation showed mCherry-positive SC-transfected cells in the ventricular, intermediate, and marginal zones (Figure 2F), whereas *Cep85l*-depleted cells failed to migrate past the intermediate zone (Figure 2G), suggesting that Cep85l acts in migrating neurons.

CEP85L Localizes to the Maternal Centriole to Control Microtubule Organization

Immunohistochemistry showed that CEP85L localizes to one of the centrioles during G1 phase of the cell cycle in U2-OS cells co-stained for Centrin, a centriolar protein (Figure 3A). We confirmed the specificity of the CEP85L antibody by immunofluorescence and western blotting using three non-overlapping siRNAs directed to CEP85L (Figures 3A and 3B). To confirm the presence of CEP85L at the centrosome, we isolated centrosomes from U2-OS cells and confirmed that CEP85L co-fractionated with the centrosomal component γ-tubulin (Figure 3C). Similar to cells in culture, CEP85L partially co-localized with the

(F) Embryonic day 14.5 mice were electroporated with mCherry and a SC or with *Cep85l #1* or *#2* shRNAs and collected at embryonic day 17.5 (E17.5). Scale bar, 100 μm.

(G) Percentage of electroporated SC or *Cep85l* shRNA-transfected mCherry-positive cells in the ventricular zone (VZ) and subventricular zone (SVZ), intermediate zone (IZ), or cortical plate (CP). At least three electroporated brains from each condition were quantified (n > 3). *p < 0.005 (Student's t test).

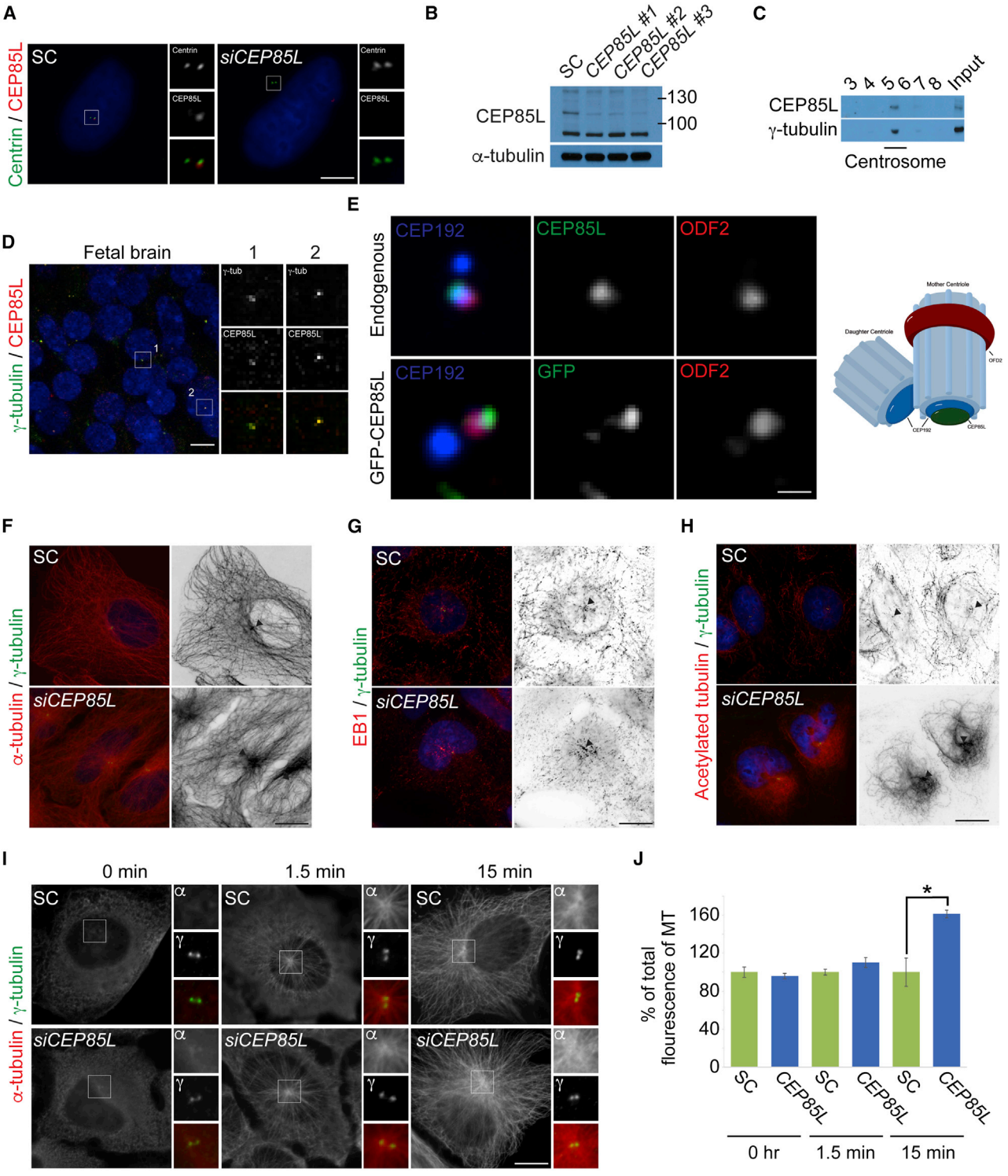

Figure 3. CEP85L Localizes to the Mother Centriole and Regulates Microtubule Cytoskeletal Organization

(A) U2-OS cells treated with SC or *CEP85L* siRNA co-stained with antibodies to Centrin (green) and CEP85L (red). The scale bar represents 5 μm for all images.

(B) Whole-cell lysate from SC and *CEP85L #1*, *#2*, or *#3* siRNA-treated U2-OS cells immunoblotted for CEP85L. Actin served as a loading control.

(C) Fractions from sucrose gradient-separated U2-OS cell lysates immunoblotted for CEP85L and γ-tubulin to identify the centrosomal fraction.

(D) Fresh-frozen GW23 fetal brains were co-stained for γ-tubulin (green) and CEP85L (red). The scale bar represents 5 μm for all images.

(legend continued on next page)

centrosomal protein γ-tubulin in GW23 fetal human brain tissue (Figure 3D). CEP85L protein levels are stable at the centrosome throughout the cell cycle (Figures S1A and S1B). Examination of endogenous CEP85L and GFP-tagged CEP85L relative to the proximal end and subdistal appendage of the mother centriole showed partial co-localization with the proximal component CEP192 but not with the subdistal centriole component ODF2 (Figure 3E), demonstrating that CEP85L localizes to the proximal end of the mother centriole, which is required for subdistal appendage organization (Mazo et al., 2016; Zhang et al., 2016).

Because subdistal appendages anchor microtubules to the mother centriole (Askham et al., 2002; Dammermann and Merdes, 2002; Delgehyr et al., 2005; Quintyne et al., 1999; Quintyne and Schroer, 2002), and the cytoskeleton is critical for neuronal migration (Lasser et al., 2018; Solecki et al., 2004), we examined whether *CEP85L*-depleted cells exhibited altered microtubule cytoskeleton organization. Although SC-treated cells displayed a radial array of microtubules originating at the centrosome, *CEP85L*-depleted cells showed overly abundant centrosomally clustered microtubules (Figure 3F). In addition, we examined the plus-end-capping protein EB1, which regulates the dynamic behavior of microtubules (Vitre et al., 2008), and found that *CEP85L*-depleted cells had increased EB1 comets in the vicinity of the centrosome (Figure 3G; Figure S1C), indicating impaired microtubule dynamics. Cellular migration depends on dynamic microtubules; therefore, we examined whether the stabilized (Yan et al., 2018; Zuo et al., 2012), acetylated microtubule cytoskeleton was disrupted upon *CEP85L* depletion. Relative to controls, *CEP85L* siRNA-treated cells exhibited increased acetylated microtubules (Figure 3H), suggesting that altered cytoskeletal dynamics may underlie the inability of *CEP85L* neurons to migrate in the developing cortex.

Given the increased centrosomal microtubules, we assessed the microtubule nucleating and anchoring ability of SC and *CEP85L* siRNA-treated cells following microtubule depolymerization. After 15 min of regrowth, SC cells formed a normal radial microtubule array originating at the centrosome (Figure 3I). In contrast, *CEP85L*-depleted cells supported a dramatic increase in microtubules anchored at the centrosome (Figure 3J). These findings suggest that the defects in microtubule organization and dynamics may explain why cells depleted of *CEP85L* are incapable of migrating.

CEP85L Localizes and Is Required to Activate CDK5 at the Mother Centriole

Immunoprecipitation of endogenous CEP85L from HeLa cells identified many co-precipitating proteins by liquid chromatography-tandem mass spectrometry (LC-MS/MS) (Table S3), including known centrosomal proteins (Jakobsen et al., 2011; Nogales-Cadenas et al., 2009) as well as products of genes essential for neuronal migration such as LIS1, NDE1, KIF2A, DYNC1H1, and CDK5 (Alkuraya et al., 2011; Bakircioglu et al., 2011; Lo Nigro et al., 1997; Magen et al., 2015; Poirier et al., 2013; Vissers et al., 2010; Figure 4A). In addition, we identified CDK5RAP2, TUBGCP3, and NEDD1, proteins required for microtubule nucleation (Choi et al., 2010; Lüders et al., 2006; Murphy et al., 1998; Tassin et al., 1998). CP110, a centriole protein (Spektor et al., 2007), served as a negative control. CEP85L interactors were sorted and prioritized based on centrosomal localization and associated mutations causing neuronal migration disorders. We confirmed specific interactions between CEP85L and LIS1, NDE1, KIF2A, and DYNC1H1 by reciprocal co-immunoprecipitation (Figures 4B and 4C), suggesting potential links of CEP85L with other genes implicated in microtubule dynamics and neuronal migration.

CEP85L-depleted cells showed normal levels of LIS proteins, although their pattern of centrosomal localization was disrupted (Figures S2A–S2C), suggesting that CEP85L functions to restrict the localization of these proteins at the centrosome. In contrast, depletion of *LIS1* and *NDE1* reduced the localization of CEP85L at the centrosome (Figure 4D; Figures S2D and S2E), whereas loss of *KIF2A* or dynein inhibition with ciliobrevin did not disrupt CEP85L localization (Figures S2D–S2G), suggesting a potential model in which CEP85L plays roles downstream of the centrosomal proteins LIS1 and NDE1 (which directly interact) (Derewenda et al., 2007) but upstream of the motor proteins KIF2A and DYNC1H1. Depletion of LIS proteins or ciliobrevin treatment did not affect the stability of CEP85L (Figures S2H and S2I), suggesting that CEP85L and its interacting proteins are not interdependent for protein stability.

The relationship of the centrosomal LIS-associated proteins and Cyclin-dependent kinase 5 (CDK5), which is also associated with cerebral cortical migration defects as well as cerebellar hypoplasia (Magen et al., 2015), has been unclear, but CEP85L may represent a key intermediary. We confirmed that CEP85L interacts with CDK5 using co-immunoprecipitation (Figure 4E) and used high-resolution imaging to show that CDK5 and active CDK5 (pCDK5) (Sharma et al., 1999) both co-localize at the proximal end of mother centrioles with CEP85L (Figure 4F). We confirmed the specificity of the CDK5 and pCDK5 antibodies in cells transfected with SC or *CDK5* siRNA (Figure S2J). Because CEP85L disrupts the localization of LIS-associated proteins, we examined the localization of CDK5 and pCDK5 in *CEP85L*-depleted cells. Unlike the relationship between CEP85L and NDE1 and LIS1, CDK5 and pCDK5 were strikingly absent from the centrosome in *CEP85L*-depleted cells (Figure 4G), suggesting that CDK5's localization requires CEP85L.

(E) Airyscan microscopy of U2-OS cells co-stained for CEP192 (blue) to mark the proximal centrioles, ODF2 (red) to mark subdistal appendages, and CEP85L (green) or GFP-CEP85L (green). The scale bar represents 1 μm for Airyscan images.
(F) Immunofluorescence analysis of SC and *CEP85L* siRNA-treated U2-OS cells co-stained with γ-tubulin (green) and α-tubulin (red).
(G) SC and *CEP85L*-depleted cells co-stained with γ-tubulin (green) and EB1 (red).
(H) U2-OS cells treated with SC or *CEP85L* siRNA were co-stained for γ-tubulin (green) and acetylated tubulin (red). Figures to the right of the merged image are inverted images of α-tubulin, EB1, or acetylated tubulin. Triangles denote the centrosome. Scale bars represent 10 μm for all images.
(I) SC and *CEP85L* siRNA-treated U2-OS cells were subjected to a microtubule regrowth assay, fixed at the indicated time points, and co-stained with α-tubulin (red) and γ-tubulin (green). The scale bar indicates 5 μm for all images.
(J) Quantification of the mean fluorescence intensities ± SD of centrosomal α-tubulin in SC and *CEP85L* siRNA-treated cells, expressed as the mean percentage ± SD of the fluorescence intensities of SC cells. For all quantifications, 10 cells were analyzed per experiment (n = 3). *p < 0.005 (Student's t test).

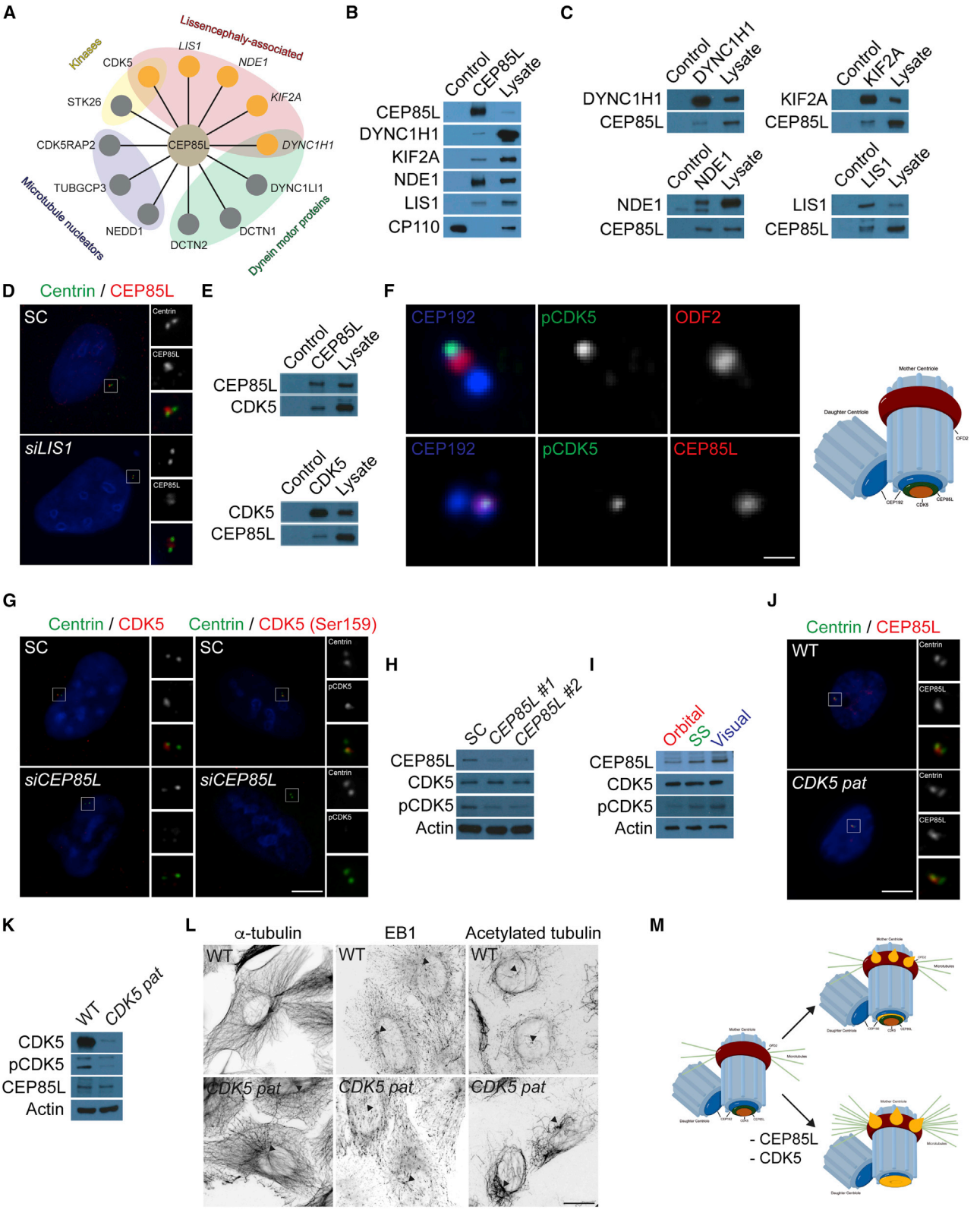

(legend on next page)

We next assessed the levels of CDK5 and pCDK5 following CEP85L depletion. Interestingly, CDK5 levels remained unchanged, but pCDK5 was dramatically decreased upon *CEP85L* knockdown (Figure 4H). Remarkably, higher levels of pCDK5 in the human visual compared with the frontal cortex paralleled the rostral-to-caudal increase in CEP85L expression (Figure 4I). Overexpression of GFP-CEP85L induces increased pCDK5 by western blot analysis and at the centrosome (Figures S2K and S2L), suggesting that CEP85L controls the localization and activation of CDK5 at the centrosome.

Because CEP85L is required to localize CDK5 to the centrosome, we investigated whether disruption of CDK5 underlies the centrosomal and cytoskeletal changes in *CEP85L*-depleted cells. We confirmed that CDK5 was lost in patient fibroblasts with a homozygous splice site variant (p.V162*fs*X19) (Magen et al., 2015), but the localization of CEP85L was unaltered (*CDK5 pat*) (Figure 4J; Figure S2M), suggesting that CEP85L is required to localize CDK5 but not vice versa. Because CDK5 interacts with LIS1, NDE1, and DYNC1H1 (Maskey et al., 2015; Pandey and Smith, 2011), we examined whether the loss of CDK5 could account for the overaccumulation of LIS proteins at the centrosome in *CEP85L*-depleted cells. As in cells depleted of *CEP85L*, *Cdk5*$^{-/-}$ mouse embryonic fibroblasts (MEFs) displayed abnormal centrosomal accumulation of *Dync1h1*, *Nde1*, *Kif2a*, and *Lis1* (Figures S2N–S2O). Similar to depletion of *CEP85L*, the levels of LIS-associated proteins were unchanged in *Cdk5*$^{-/-}$ cells (Figure S2P). Disorganization of LIS proteins was also observed in *CDK5* patient fibroblasts and *CDK5*-depleted U2OS cells (data not shown). These findings suggest a role of CDK5 in organizing LIS proteins at the centrosome downstream of CEP85L.

To confirm that the cytoskeletal defects observed in *CEP85L*-depleted cells reflect disrupted CDK5, we examined microtubule organization in *CDK5* patient and *Cdk5*$^{-/-}$ cells. Similar to *CEP85L* siRNA-transfected cells, patient fibroblasts and *Cdk5*$^{-/-}$ MEFs exhibited increased centrosomal microtubules, EB1, and acetylated microtubules, strongly suggesting that the disruption of the cytoskeleton in *CEP85L*-depleted cells is due to disrupted CDK5 activity (Figures 4L and 4M; Figures S2Q and S2R). To confirm that CDK5 activity is required to organize LIS proteins at the centrosome, we treated cells with the CDK5/1/2 inhibitor roscovitine at 20 μM to selectively inhibit CDK5. Inhibition of CDK5 activity did not alter the localization of active CDK5 at the centrosome (Figures S2S and S2U). However, roscovitine-treated cells exhibited increased centrosomal DYNC1H1, KIF2A, NDE1, and LIS1, similar to loss of *CEP85L* or *CDK5* (Figures S2T and S2U). The levels of the LIS proteins were unaltered because of inhibition of CDK5 activity (Figure S2V). Taken together, these findings suggest that CEP85L localizes and activates CDK5 at the centrosome to control centrosome and cytoskeleton organization.

DISCUSSION

We present seven individuals from seven families with mutations in *CEP85L* with strikingly similar radiographical and clinical features. The missense mutations identified in CEP85L were constrained to a 10-amino-acid stretch of a single constrained exon, suggesting that this region is intolerant to alterations and may represent a highly critical domain for CEP85L function. Because healthy individuals can tolerate LoF and truncation mutations in other CEP85L exons, the missense mutations may affect a binding domain in CEP85L critical for function. Alternatively, this clustering of missense variants and the recurrent splicing variant suggest that some mutations could act by a dominant-negative mechanism. Additional studies are required to determine the pathogenic mechanism of *CEP85L* mutations.

Figure 4. CEP85L Is Required to Localize and Activate the LIS Protein CDK5

(A) Schematic of centrosomal CEP85L-interacting proteins identified by endogenous immunoprecipitation of CEP85L followed by LC-MS/MS analysis. Interactors were sorted and prioritized based on centrosomal localization and disease association.

(B) Immunoprecipitated endogenous CEP85L and CP110 from HeLa cell lysates was immunoblotted for co-precipitating proteins for CEP85L, DYNC1H1, KIF2A, NDE1, and LIS1. CP110 served as a negative control throughout. Lysate represents 5% of the total cell lysate used in the immunoprecipitation assays.

(C) HeLa cell lysate was subjected to immunoprecipitation of DYNC1H1, KIF2A, NDE1, and LIS1. Precipitating proteins were immunoblotted for CEP85L, DYNC1H1, KIF2A, NDE1, and LIS1.

(D) U2-OS cells transfected with siRNA to SC or *LIS1* co-stained with Centrin (green) and CEP85L (red).

(E) HeLa cell lysate was subjected to immunoprecipitation of CEP85L, CDK5, and CP110, which served as a negative control. Precipitating proteins were immunoblotted for CEP85L and CDK5.

(F) Airyscan maximum projections of U2-OS cells co-stained with antibodies to pCDK5 (green), ODF2 (red, to mark the subdistal appendages of mother centrioles), CEP85L (red), and CEP192 (blue, to mark the proximal domains of the centrioles). The scale bar represents 1 μm for Airyscan images.

(G) Immunofluorescence of SC and *CEP85L* siRNA-transfected U2-OS cells co-stained for Centrin (green) and CDK5 (red) or pCDK5 (red). The scale bars represents 5 μm for all images.

(H) Total cell lysates from U2-OS cells transfected with SC and *CEP85L #1* or *#2* probed with antibodies to CEP85L, CDK5, and pCDK5. Actin served as a loading control.

(I) Whole-cell lysate from the posterior frontal, parietal, and occipital lobes of a GW23 human fetus blotted for CEP85L, CDK5, and pCDK5. Actin served as a loading control.

(J) WT and *CDK5* patient fibroblasts (p.V162*fs*X19, *CDK5 pat*) co-stained with antibodies to Centrin (green) and pCDK5 (red).

(K) Whole-cell lysate from WT or *CDK5* patient fibroblasts probed with antibodies to CDK5, pCDK5, and CEP85L. Actin served as a loading control.

(L) Inverted images of WT and *CDK5* patient cells stained with α-tubulin, EB1, or acetylated tubulin. Triangles denote the centrosome. The scale bars represents 10 μm for all images.

(M) CEP85L (green) localizes CDK5 (beige) to the proximal end of mother centrioles (CEP192, blue) to be activated. At the centrosome, CDK5 activity restricts the accumulation of LIS-associated proteins (orange) that localize to the proximal mother centriole and its subdistal appendages. Consequently, loss of CEP85L or CDK5 causes excessive localization of LIS proteins, resulting in excessive anchoring of microtubules at the mother centriole, leading to cells incapable of migrating.

CEP85L is an important component of the neuronal migration machinery, and disruption of CEP85L results in abnormal posterior cortical architecture, paralleling the higher levels of CEP85L expressed in the posterior cortex. We demonstrate that CEP85L associates with CDK5 at the centrosome to promote its activation and to organize centrosomal LIS-associated proteins (Figure 4N). Taken together, we demonstrate that CEP85L promotes CDK5 localization and activation at the centrosome to form a dynamic microtubule cytoskeleton required for neuronal migration in the developing cortex.

STAR★METHODS

Detailed methods are provided in the online version of this paper and include the following:

- KEY RESOURCES TABLE
- LEAD CONTACT AND MATERIALS AVAILABILITY
- EXPERIMENTAL MODEL AND SUBJECT DETAILS
  - Human subjects
  - Animal Use
- METHOD DETAILS
  - Quantitative PCR
  - Molecular biology
  - Cell culture
  - Centrosome enrichment
  - Western blotting and immunoprecipitation
  - Mass spectrometry analysis
  - Immunostaining
  - Migration assay
  - Microtubule regrowth assay
  - In utero electroporation of mouse embryos
- QUANTIFICATION AND STATISTICAL ANALYSIS
- DATA AND CODE AVAILABILITY

SUPPLEMENTAL INFORMATION

Supplemental Information can be found online at https://doi.org/10.1016/j.neuron.2020.01.030.

ACKNOWLEDGMENTS

The authors thank the families for their invaluable participation in our study. We thank Drs. Douglas Lowy, Brajendra Tripathi, Daniella Magen, and Andrew Holland for cell lines and antibodies. We also thank Drs. Meng-Fu Bryan Tsou and Laurence Pelletier for insightful discussions. C.A.W. was supported by The Manton Center for Orphan Disease Research, R01NS035129 and R01NS032457 from the NINDS, and the Allen Discovery Center program through The Paul G. Allen Frontiers Group. C.A.W. is an Investigator of the Howard Hughes Medical Institute. A.K. was supported by R21NS104633-01A1, the William Randolph Hearst Fund, and the Charles Hood Foundation. A.O. was supported by the K12 HD052896 Child Health Research Career Development Award Program. E.S. was supported by NIH T32GM007753 and the HCBI Simmons Award. Sequencing and analysis for PAC2801, LIS6801, DC7401, and PAC3301 were provided by the Broad Institute of MIT and Harvard Center for Mendelian Genomics (Broad CMG) and were funded by the National Human Genome Research Institute, the National Eye Institute, and National Heart, Lung and Blood Institute grant UM1 HG008900 (to Daniel MacArthur and Heidi Rehm). A.B. was supported by GNT1113531 from the Australian Genomics Health Alliance and NHMRC, a Maurice de Rohan international scholarship, and an Australian Government Research Training Program scholarship. GeneDx Inc. performed a trio exome on LIS7901, and a connection was made via MatchMaker Exchange. The work done for 40291IMID was supported by the National Science Centre, Poland 2015/19/B/NZ2/01824 (to W.W.), and exome sequencing was performed at the Human Genome Sequencing Center (HGSC) at Baylor College of Medicine through the Baylor-Hopkins Center for Mendelian Genomics (BHCMG) initiative. The content is solely the responsibility of the authors and does not necessarily represent the official views of the NIH.

AUTHOR CONTRIBUTIONS

The project was conceived by A.K. and C.A.W., and the experiments were carried out by A.K. C.K. and A.L. had comparable contributions to this study regarding cell biology and genetics, respectively. D.M.G. and L.I. performed *in utero* electroporation. E.S. performed qPCR in human tissue. G.M.S. helped analyze scratch wound assays. Participant enrollment, sample collection, and phenotype review were performed by A.L., J.N.P., A.B.B., A.J.B., E.Y., R.S.H., P.G., W.W., J.S.C., S.A.F., C.J.Y., M.S., K.W.B., D.G.V., and C.A.W. Data analysis was performed by A.K., C.K., D.M.G., G.M.S., and L.I. The manuscript was written by A.K. with help from the other authors. All aspects of the study were supervised by A.K. and C.A.W.

DECLARATION OF INTERESTS

C.A.W. serves on advisory boards for the Allen Brain Institute, Third Rock Ventures, and Maze Therapeutics and on editorial boards for Annals of Neurology, Trends in Neurosciences, and neuroDEVELOPMENTS. M.S. received research funding from Roche, Novartis, Pfizer, LAM Therapeutics, and Quadrant Biosciences; has served on the scientific advisory boards of Sage Therapeutics, Roche, Takeda, Celgene, and the PTEN Research Foundation; and serves on the Board of the Tuberous Sclerosis Alliance. All of these activities are outside of the submitted manuscript. J.S.C. is a consultant for Invitae. D.V. serves as a consultant to SK Life Science and Otsuka Pharmaceuticals, is on the speaker's bureaus for UCB and Greenwich Pharmaceuticals, and conducts industry-supported clinical drug trials for SK Life Science, Biogen, and UCB Pharmaceuticals. K.M. is an employee of GeneDX, Inc.

Received: September 6, 2019
Revised: November 22, 2019
Accepted: January 22, 2020
Published: February 24, 2020

REFERENCES

Alkuraya, F.S., Cai, X., Emery, C., Mochida, G.H., Al-Dosari, M.S., Felie, J.M., Hill, R.S., Barry, B.J., Partlow, J.N., Gascon, G.G., et al. (2011). Human mutations in NDE1 cause extreme microcephaly with lissencephaly [corrected]. Am. J. Hum. Genet. *88*, 536–547.

Askham, J.M., Vaughan, K.T., Goodson, H.V., and Morrison, E.E. (2002). Evidence that an interaction between EB1 and p150(Glued) is required for the formation and maintenance of a radial microtubule array anchored at the centrosome. Mol. Biol. Cell *13*, 3627–3645.

Bakircioglu, M., Carvalho, O.P., Khurshid, M., Cox, J.J., Tuysuz, B., Barak, T., Yilmaz, S., Caglayan, O., Dincer, A., Nicholas, A.K., et al. (2011). The essential role of centrosomal NDE1 in human cerebral cortex neurogenesis. Am. J. Hum. Genet. *88*, 523–535.

Choi, Y.K., Liu, P., Sze, S.K., Dai, C., and Qi, R.Z. (2010). CDK5RAP2 stimulates microtubule nucleation by the gamma-tubulin ring complex. J. Cell Biol. *191*, 1089–1095.

Dammermann, A., and Merdes, A. (2002). Assembly of centrosomal proteins and microtubule organization depends on PCM-1. J. Cell Biol. *159*, 255–266.

Delgehyr, N., Sillibourne, J., and Bornens, M. (2005). Microtubule nucleation and anchoring at the centrosome are independent processes linked by ninein function. J. Cell Sci. *118*, 1565–1575.

Derewenda, U., Tarricone, C., Choi, W.C., Cooper, D.R., Lukasik, S., Perrina, F., Tripathy, A., Kim, M.H., Cafiso, D.S., Musacchio, A., and Derewenda, Z.S.

(2007). The structure of the coiled-coil domain of Ndel1 and the basis of its interaction with Lis1, the causal protein of Miller-Dieker lissencephaly. Structure *15*, 1467–1481.

de Rie, D., Abugessaisa, I., Alam, T., Arner, E., Arner, P., Ashoor, H., Åström, G., Babina, M., Bertin, N., Burroughs, A.M., et al. (2017). An Integrated Expression Atlas of miRNAs and Their Promoters in Human and Mouse. Nat. Biotechnol. *35*, 872–878.

Di Donato, N., Chiari, S., Mirzaa, G.M., Aldinger, K., Parrini, E., Olds, C., Barkovich, A.J., Guerrini, R., and Dobyns, W.B. (2017). Lissencephaly: Expanded imaging and clinical classification. Am. J. Med. Genet. A. *173*, 1473–1488.

Di Donato, N., Timms, A.E., Aldinger, K.A., Mirzaa, G.M., Bennett, J.T., Collins, S., Olds, C., Mei, D., Chiari, S., Carvill, G., et al.; University of Washington Center for Mendelian Genomics (2018). Analysis of 17 genes detects mutations in 81% of 811 patients with lissencephaly. Genet. Med. *20*, 1354–1364.

Guerrini, R., Barkovich, A.J., Sztriha, L., and Dobyns, W.B. (2000). Bilateral frontal polymicrogyria: a newly recognized brain malformation syndrome. Neurology *54*, 909–913.

Havrilla, J.M., Pedersen, B.S., Layer, R.M., and Quinlan, A.R. (2019). A map of constrained coding regions in the human genome. Nat. Genet. *51*, 88–95.

Jakobsen, L., Vanselow, K., Skogs, M., Toyoda, Y., Lundberg, E., Poser, I., Falkenby, L.G., Bennetzen, M., Westendorf, J., Nigg, E.A., et al. (2011). Novel asymmetrically localizing components of human centrosomes identified by complementary proteomics methods. EMBO J. *30*, 1520–1535.

Jamuar, S.S., Lam, A.T., Kircher, M., D'Gama, A.M., Wang, J., Barry, B.J., Zhang, X., Hill, R.S., Partlow, J.N., Rozzo, A., et al. (2014). Somatic mutations in cerebral cortical malformations. N. Engl. J. Med. *371*, 733–743.

Johnson, M.B., Wang, P.P., Atabay, K.D., Murphy, E.A., Doan, R.N., Hecht, J.L., and Walsh, C.A. (2015). Single-cell analysis reveals transcriptional heterogeneity of neural progenitors in human cortex. Nat. Neurosci. *18*, 637–646.

Kodani, A., Yu, T.W., Johnson, J.R., Jayaraman, D., Johnson, T.L., Al-Gazali, L., Sztriha, L., Partlow, J.N., Kim, H., Krup, A.L., et al. (2015). Centriolar satellites assemble centrosomal microcephaly proteins to recruit CDK2 and promote centriole duplication. eLife *4*.

Lasser, M., Tiber, J., and Lowery, L.A. (2018). The Role of the Microtubule Cytoskeleton in Neurodevelopmental Disorders. Front. Cell. Neurosci. *12*, 165.

Lee, M.K., Tuttle, J.B., Rebhun, L.I., Cleveland, D.W., and Frankfurter, A. (1990). The expression and posttranslational modification of a neuron-specific beta-tubulin isotype during chick embryogenesis. Cell Motil. Cytoskeleton *17*, 118–132.

Lek, M., Karczewski, K.J., Minikel, E.V., Samocha, K.E., Banks, E., Fennell, T., O'Donnell-Luria, A.H., Ware, J.S., Hill, A.J., Cummings, B.B., et al.; Exome Aggregation Consortium (2016). Analysis of protein-coding genetic variation in 60,706 humans. Nature *536*, 285–291.

Lo Nigro, C., Chong, C.S., Smith, A.C., Dobyns, W.B., Carrozzo, R., and Ledbetter, D.H. (1997). Point mutations and an intragenic deletion in LIS1, the lissencephaly causative gene in isolated lissencephaly sequence and Miller-Dieker syndrome. Hum. Mol. Genet. *6*, 157–164.

Lüders, J., Patel, U.K., and Stearns, T. (2006). GCP-WD is a gamma-tubulin targeting factor required for centrosomal and chromatin-mediated microtubule nucleation. Nat. Cell Biol. *8*, 137–147.

Magen, D., Ofir, A., Berger, L., Goldsher, D., Eran, A., Katib, N., Nijem, Y., Vlodavsky, E., Tzur, S., Behar, D.M., et al. (2015). Autosomal recessive lissencephaly with cerebellar hypoplasia is associated with a loss-of-function mutation in CDK5. Hum. Genet. *134*, 305–314.

Maskey, D., Marlin, M.C., Kim, S., Kim, S., Ong, E.C., Li, G., and Tsiokas, L. (2015). Cell cycle-dependent ubiquitylation and destruction of NDE1 by CDK5-FBW7 regulates ciliary length. EMBO J. *34*, 2424–2440.

Mazo, G., Soplop, N., Wang, W.J., Uryu, K., and Tsou, M.F. (2016). Spatial Control of Primary Ciliogenesis by Subdistal Appendages Alters Sensation-Associated Properties of Cilia. Dev. Cell *39*, 424–437.

Murphy, S.M., Urbani, L., and Stearns, T. (1998). The mammalian gamma-tubulin complex contains homologues of the yeast spindle pole body components spc97p and spc98p. J. Cell Biol. *141*, 663–674.

Nogales-Cadenas, R., Abascal, F., Díez-Pérez, J., Carazo, J.M., and Pascual-Montano, A. (2009). CentrosomeDB: a human centrosomal proteins database. Nucleic Acids Res. *37*, D175–D180.

Pandey, J.P., and Smith, D.S. (2011). A Cdk5-dependent switch regulates Lis1/Ndel1/dynein-driven organelle transport in adult axons. J. Neurosci. *31*, 17207–17219.

Paridaen, J.T., Wilsch-Bräuninger, M., and Huttner, W.B. (2013). Asymmetric inheritance of centrosome-associated primary cilium membrane directs ciliogenesis after cell division. Cell *155*, 333–344.

Poirier, K., Lebrun, N., Broix, L., Tian, G., Saillour, Y., Boscheron, C., Parrini, E., Valence, S., Pierre, B.S., Oger, M., et al. (2013). Mutations in TUBG1, DYNC1H1, KIF5C and KIF2A cause malformations of cortical development and microcephaly. Nat. Genet. *45*, 639–647.

Quintyne, N.J., and Schroer, T.A. (2002). Distinct cell cycle-dependent roles for dynactin and dynein at centrosomes. J. Cell Biol. *159*, 245–254.

Quintyne, N.J., Gill, S.R., Eckley, D.M., Crego, C.L., Compton, D.A., and Schroer, T.A. (1999). Dynactin is required for microtubule anchoring at centrosomes. J. Cell Biol. *147*, 321–334.

Rakic, P. (1971). Neuron-glia relationship during granule cell migration in developing cerebellar cortex. A Golgi and electronmicroscopic study in Macacus Rhesus. J. Comp. Neurol. *141*, 283–312.

Retterer, K., Juusola, J., Cho, M.T., Vitazka, P., Millan, F., Gibellini, F., Vertino-Bell, A., Smaoui, N., Neidich, J., Monaghan, K.G., et al. (2016). Clinical application of whole-exome sequencing across clinical indications. Genet. Med. *18*, 696–704.

Saito, T. (2006). In vivo electroporation in the embryonic mouse central nervous system. Nat. Protoc. *1*, 1552–1558.

Sharma, P., Sharma, M., Amin, N.D., Albers, R.W., and Pant, H.C. (1999). Regulation of cyclin-dependent kinase 5 catalytic activity by phosphorylation. Proc. Natl. Acad. Sci. USA *96*, 11156–11160.

Solecki, D.J., Model, L., Gaetz, J., Kapoor, T.M., and Hatten, M.E. (2004). Par6alpha signaling controls glial-guided neuronal migration. Nat. Neurosci. *7*, 1195–1203.

Spektor, A., Tsang, W.Y., Khoo, D., and Dynlacht, B.D. (2007). Cep97 and CP110 suppress a cilia assembly program. Cell *130*, 678–690.

Tassin, A.M., Celati, C., Moudjou, M., and Bornens, M. (1998). Characterization of the human homologue of the yeast spc98p and its association with gamma-tubulin. J. Cell Biol. *141*, 689–701.

Vissers, L.E., de Ligt, J., Gilissen, C., Janssen, I., Steehouwer, M., de Vries, P., van Lier, B., Arts, P., Wieskamp, N., del Rosario, M., et al. (2010). A de novo paradigm for mental retardation. Nat. Genet. *42*, 1109–1112.

Vitre, B., Coquelle, F.M., Heichette, C., Garnier, C., Chrétien, D., and Arnal, I. (2008). EB1 regulates microtubule dynamics and tubulin sheet closure in vitro. Nat. Cell Biol. *10*, 415–421.

Yan, B., Xie, S., Liu, Y., Liu, W., Li, D., Liu, M., Luo, H.R., and Zhou, J. (2018). Histone deacetylase 6 modulates macrophage infiltration during inflammation. Theranostics *8*, 2927–2938.

Yang, Y.J., Baltus, A.E., Mathew, R.S., Murphy, E.A., Evrony, G.D., Gonzalez, D.M., Wang, E.P., Marshall-Walker, C.A., Barry, B.J., Murn, J., et al. (2012). Microcephaly gene links trithorax and REST/NRSF to control neural stem cell proliferation and differentiation. Cell *151*, 1097–1112.

Zhang, X., Chen, M.H., Wu, X., Kodani, A., Fan, J., Doan, R., Ozawa, M., Ma, J., Yoshida, N., Reiter, J.F., et al. (2016). Cell-Type-Specific Alternative Splicing Governs Cell Fate in the Developing Cerebral Cortex. Cell *166*, 1147–1162.e15.

Zuo, Q., Wu, W., Li, X., Zhao, L., and Chen, W. (2012). HDAC6 and SIRT2 promote bladder cancer cell migration and invasion by targeting cortactin. Oncol. Rep. *27*, 819–824.

STAR★METHODS

KEY RESOURCES TABLE

REAGENT or RESOURCE	SOURCE	IDENTIFIER
Antibodies		
CEP85L	Proteintech	Cat# 24588-1-AP
LIS1	Sigma	Cat# SAB2500597; RRID: AB_10604255
TUJ1	Proteintech	Cat#66375-1-Ig
β-actin	Proteintech	Cat# 20536-1-AP; RRID: AB_10700003
α-tubulin	Sigma	Cat# T6074; RRID: AB_261690
Centrin	Sigma	Cat# 04-1624; RRID: AB_10563501
ODF2	Abnova	Cat# H00004957-M01; RRID: AB_1137338
γ-tubulin	Sigma	Cat# T5192; RRID: AB_477582
pHH3	Cell Signal	Cat# 9701S; RRID: AB_331535
CEP192 Alexa647	Andrew Holland	PMID: 31115335
Acetylated tubulin	Sigma	Cat# T6793; RRID: AB_477585
EB1	BD Biosciences	Cat# 610535; RRID: AB_397892
DYNC1H1	Proteintech	Cat# 12345-1-AP; RRID: AB_2261765
DYNC1H1	Bethyl Labs	Cat# A304-720A; RRID: AB_2620915
KIF2A	Thermo Fisher	Cat# PA3-16833; RRID: AB_2131873
CP110	Proteintech	Cat# 12780-1-AP; RRID: AB_10638480
NDE1	Proteintech	Cat# 10233-1-AP; RRID: AB_2149877
CDK5	Cell Signal	Cat# 2506S; RRID: AB_2078855
CDK5	Santa Cruz Biotechnology	Cat# sc-6247; RRID: AB_627241
pCDK5 (Ser159)	Santa Cruz Biotechnology	Cat# sc-377558
pCDK5 (Ser159)	Thermo Fisher	Cat# PA5-64751; RRID: AB_2663116
Centrin1	Proteintech	Cat# 12794-1-AP; RRID: AB_2077371
GFP-HRP	Cell Signal	Cat# 2037S; RRID: AB_1281301
Native IgG HRP	Cell Signal	Cat# 5127S; RRID: AB_10892860
Biological Samples		
23 week gestational fetal brain	Massachusetts General Hospital	N/A
Chemicals, Peptides, and Recombinant Proteins		
Ciliobrevin D	Sigma	Cat# 250401
Nocodazole	Sigma	Cat# M1404
DMSO	Sigma	Cat# 472301
Thymidine	Sigma	Cat# T1895
Roscovitine	Sigma	Cat# R7772
Mycoplasma Removal Agent	Bio-Rad	Cat# BUF035
Lipofectamine3000	Thermo Fisher	Cat# L30000
Lipofectamine RNAiMAX	Thermo Fisher	Cat# 13778150
Experimental Models: Cell Lines		
U2-OS	ATCC	CVCL_0042
HeLa	ATCC	CVCL_0030
Neuro-2a	ATCC	CVCL_0470
WT MEFs (mouse embryonic fibroblasts)	Dr. Douglas Lowy (NIH)	PMID: 25452387
Cdk5$^{-/-}$ MEFs (mouse embryonic fibroblasts)	Dr. Douglas Lowy (NIH)	PMID: 25452387
WT fibroblasts	Daniella Magen (Ruth Rappaport Children's Hospital)	PMID: 25560765

(*Continued on next page*)

Continued

REAGENT or RESOURCE	SOURCE	IDENTIFIER
CDK5 patient fibroblasts	Daniella Magen (Ruth Rappaport Children's Hospital)	PMID: 25560765
Experimental Models: Organisms/Strains		
Crl:CD-1 laboratory mouse	Charles River	Cat# 5652673; RRID: MGI:5652673
Oligonucleotides		
siRNA targeting sequence: CEP85L #1: GGCCACTTCGGAAATGGTCATCTTT	Thermo Fisher	Cat#: HSS139769
siRNA targeting sequence: CEP85L #2: GGCCACTTCGGAAATGGTCATCTTT	Thermo Fisher	Cat#: HSS139770
siRNA targeting sequence: CEP85L #3: GGCCACTTCGGAAATGGTCATCTTT	Thermo Fisher	Cat#: HSS180226
siRNA targeting sequence: LIS1 #1: GGTACGTATGGTACGGCCAAATCAA	Thermo Fisher	Cat#: HSS107554
siRNA targeting sequence: LIS1 #2: TGAAGCAACAGGATCTGAGACTAAA	Thermo Fisher	Cat#: HSS107555
siRNA targeting sequence: LIS1 #3: CCAGAGACAACGAGATGAACTAAAT	Thermo Fisher	Cat#: HSS107556
siRNA targeting sequence: NDE1 #1: GGAAACCATCAAGGAGAAGTTTGAA	Thermo Fisher	Cat#: HSS123304
siRNA targeting sequence: NDE1 #2: GAGCAAGCAAATGACGACCTGGAAA	Thermo Fisher	Cat#: HSS123305
siRNA targeting sequence: NDE1 #3: ACCGAGGACCCAGCTCAAGTTTAAA	Thermo Fisher	Cat#: HSS123306
siRNA targeting sequence: KIF2A #1: CCCTGACCTTGTTCCTGATGAAGAA	Thermo Fisher	Cat#: HSS105799
siRNA targeting sequence: KIF2A #2: GAGACTTTAGAGGAAGTTTGGATTA	Thermo Fisher	Cat#: HSS105800
siRNA targeting sequence: KIF2A #3: CCTAATGAAATGGTTTACAGGTTTA	Thermo Fisher	Cat#: HSS180178
siRNA targeting sequence: CDK5 #1: GGTGACCTCGATCCTGAGATTGTAA	Thermo Fisher	Cat#: HSS101729
siRNA targeting sequence: CDK5 #2: GGCAATGATGTCGATGACCAGTTGA	Thermo Fisher	Cat#: HSS101730
siRNA targeting sequence: CDK5 #3: GATTCTGTCATAGCCGCAATGTGCT	Thermo Fisher	Cat#: HSS173470
Scramble Control: AAACTAAACTGAGGCAATGCC	Thermo Fisher	N/A
CEP85L.EcoR1: GATTAGGAATTCGATGTGGGGGC GCTTCC	Thermo Fisher	N/A
CEP85L.BamH1: TCTTCTGGATCCTCACTGAGTAAT GCAGTTGTCTCC	Thermo Fisher	N/A
shRNA.Scramble.F: CACCGAAACTAAA CTGAGGCAATGCCCGAAGGCATT GCCTCAGTTTAG	Thermo Fisher	N/A
shRNA.Scramble.R: AAAACTAAAC TGAGGCAATGCCTTCGGGCATTGCC TCAGTTTAGTTTC	Thermo Fisher	N/A
shRNA.Cep85l.1.F: CACCGCTTCCG TTTCCAAACATAGGCGAACCTATG TTTGGAAACGGAAGC	Thermo Fisher	N/A

(*Continued on next page*)

Continued

REAGENT or RESOURCE	SOURCE	IDENTIFIER
shRNA.Cep85l.1.R: AAAAGCTTCCG TTTCCAAACATAGGTTCGCCTATG TTTGGAAACGGAAGC	Thermo Fisher	N/A
shRNA.Cep85l.2.F: CACCGCTGGGAA TCCGATCAATGACGAATCA TTGATCGGATTCCCAG	Thermo Fisher	N/A
shRNA.Cep85l.2.R: AAAACTGGGAA TCCGATCAATGATTCGTCATTGATC GGATTCCCAGC	Thermo Fisher	N/A
qPCR.Cep85l.F: CAAGCCTAGTCGATCATTGGTC	Thermo Fisher	N/A
qPCR.Cep85l.R: AGATTCCCTATGTTTGGAAACGG	Thermo Fisher	N/A
qPCR.Actb: GGCTGTATTCCCCTCCATCG	Thermo Fisher	N/A
qPCR.Actb: CCAGTTGGTAACAATGCCATGT	Thermo Fisher	N/A
Recombinant DNA		
pEGFP-C1	Clontech	Cat# 6084-1
pEGFP-CEP85L	Self	Self
mCherry-C1	Self	Self
BLOCK-IT U6	Thermo Fisher	Cat# K494500
pcDNA-DEST53	Thermo Fisher	Cat# 12288015
Software and Algorithms		
Adobe Illustrator 2019	Adobe	RRID: SCR_010279
Adobe Photoshop 2019	Adobe	RRID: SCR_014199
FIJI	FIJI	RRID: SCR_002285

LEAD CONTACT AND MATERIALS AVAILABILITY

Further information and requests for resources and reagents should be directed to and will be fulfilled by the Lead Contact, Dr. Christopher A. Walsh (christopher.walsh@childrens.harvard.edu)

EXPERIMENTAL MODEL AND SUBJECT DETAILS

Human subjects

Peripheral blood samples from the affected individuals and parents were analyzed by whole-exome sequencing (WES). This study was approved by the institutional review boards of Boston Children's Hospital and Beth Israel Deaconess Medical Center. Subjects were identified and evaluated in a clinical setting, and biological samples were collected for research purposes after obtaining written informed consent. 40291IMID was investigated via protocol approved by the institutional review boards for the protection of human subjects at the Institute of Mother and Child (Warsaw, Poland). The cases in this cohort were ascertained and processed using a variety of different methods.

Whole exome sequencing and data processing for PAC2801, LIS6801, DC7401, and PAC3301 was performed by the Genomics Platform at the Broad Institute of Harvard and MIT (Broad Institute, Cambridge, MA, USA). We performed whole exome sequencing on DNA samples (> 250 ng of DNA, at > 2 ng/ul) using Illumina exome capture (38 Mb target). Our exome-sequencing pipeline included sample plating, library preparation (2-plexing of samples per hybridization), hybrid capture, sequencing (150 bp paired reads), sample identification QC check, and data storage. Our hybrid selection libraries cover > 90% of targets at 20x and a mean target coverage of ~100x. The exome sequencing data was de-multiplexed and each sample's sequence data were aggregated into a single Picard BAM file. Exome sequencing data was processed through a pipeline based on Picard, using base quality score recalibration and local realignment at known indels. We used the BWA aligner for mapping reads to the human genome build 37 (hg19). Single Nucleotide Polymorphism (SNPs) and insertions/deletions (indels) were jointly called across all samples using Genome Analysis Toolkit (GATK) HaplotypeCaller package version 3.4. Default filters were applied to SNP and indel calls using the GATK Variant Quality Score Recalibration (VQSR) approach. Lastly, the variants were annotated using Variant Effect Predictor (VEP).

For additional information please refer to Supplementary Section 1 of the paper describing ExAC (Lek et al., 2016). The variant call set was uploaded on to Seqr and analysis was performed using the various inheritance patterns. A custom panel of genes known to be related to neuronal migration was generated and cases with variants in known genes were filtered out. Candidate variants were validated further by Sanger sequencing.

LIS7901 was enrolled through the Walsh laboratory, however sequencing was performed via GeneDx, Inc. GeneDx performed trio exome on this individual and a connection was made via Matchbox. Using genomic DNA from the proband and parents, the exonic regions and flanking splice junctions of the genome were captured using the IDT xGen Exome Research Panel v1.0. Massively parallel (NextGen) sequencing was done on an Illumina system with 100bp or greater paired-end reads. Reads were aligned to human genome build GRCh37/UCSC hg19, and analyzed for sequence variants using a custom-developed analysis tool. Additional sequencing technology and variant interpretation protocol has been previously described (Retterer et al., 2016). The general assertion criteria for variant classification are publicly available on the GeneDx ClinVar submission page (https://www.ncbi.nlm.nih.gov/clinvar/submitters/26957/)

40291IMID's DNA was isolated from clotted whole blood by using the Clotspin Baskets and the Gentra PureGene Blood kit (QIAGEN) according to the manufacturer's instructions. WES was performed at the Human Genome Sequencing Center (HGSC) at Baylor College of Medicine through the Baylor-Hopkins Center for Mendelian Genomics (BHCMG) initiative. Using 1 μg of DNA an Illumina paired-end pre-capture library was constructed according to the manufacturer's protocol (Illumina Multiplexing_SamplePrep_Guide_1005361_D) with modifications as described in the BCM-HGSC Illumina Barcoded Paired-End Capture Library Preparation protocol. Pre-capture libraries were pooled into 4-plex library pools and then hybridized in solution to the HGSC-designed Core capture reagent (52 Mb, NimbleGen) or 6-plex library pools used the custom VCRome 2.1 capture reagent (42 Mb, NimbleGen) according to the manufacturer's protocol (NimbleGen SeqCap EZ Exome Library SR User's Guide) with minor revisions. The sequencing run was performed in paired-end mode using the Illumina HiSeq 2000 platform, with sequencing-by-synthesis reactions extended for 101 cycles from each end and an additional 7 cycles for the index read. With a sequencing yield of 8.6 Gb, the sample achieved 94% of the targeted exome bases covered to a depth of 20 × or greater. Illumina sequence analysis was performed using the HGSC Mercury analysis pipeline (https://www.hgsc.bcm.edu/software/mercury) which moves data through various analysis tools from the initial sequence generation on the instrument to annotated variant calls (SNPs and intra-read in/dels). The ACMG guidance for interpretation of sequence variants identified in known disease genes was applied (Table S1). Variants in candidate genes were considered pathogenic or potentially pathogenic based on: (i) variant frequency in the in-house and public mutation databases, (ii) bioinformatics analysis with application of predictive programs, (iii) genotype–phenotype correlation analysis, (iv) familial segregation studies, and (v) functional studies—if available. Identified variants were deposited into the ClinVar database (https://login.ezp-prod1.hul.harvard.edu/login?qurl=https://www.ncbi.nlm.nih.gov%2fclinvar%2f); consecutive accession numbers SCV000598581–SCV000598612.

Animal Use

Mouse experiments were carried out humanly and approved by Boston Children's Hospital IACUC protocols. Mice were electroporated at embryonic day 14.5 and processed on day 17.5.

METHOD DETAILS

Quantitative PCR

RNA was isolated using the RNeasy kit (QIAGEN) and reverse transcribed using SuperScript IV First-Strand Synthesis System (Life Technologies). Isolated cDNA was quantified using PowerUp SYBR Green Master Mix (Life Technologies) according to manufacturer's instructions using a StepOnePlus Real-Time PCR System (Thermo Fisher). All primers (Thermo Fisher) for qPCR were generated using the Mass General Hospital/Harvard Medical School PrimerBank. All quantifications were normalized to β-actin.

Molecular biology

Human *CEP85L* cDNA (ENST00000368491) was PCR-amplified from HeLa cell cDNA and cloned into the eGFP-C1 plasmid (Clonetech). To generate the scrambled control and *Cep85L* shRNA constructs oligos were hybridized and closed into BLOCK-iT U6 RNAi Entry Vector Kit (Life Technologies). Constructs were subsequently cloned into pcDNA-DEST53 Vector Life Technologies). The mCherry-C1 construct was generated by PCR amplifying mCherry (gift of Dr. Roger Tsien) into the eGFP-C1 plasmid.

Cell culture

U2-OS and HeLa cells were maintained in Advanced DMEM (Life Technologies) supplemented with 3% fetal bovine serum (FBS, Life Technologies and Atlanta Biologics) and GlutaMax-I (Life Technologies). N2A cells were grown in DMEM supplemented with 10% FBS and GlutaMAX-I. Wild-type and *Cdk5*$^{-/-}$ mouse embryonic fibroblasts (gift from Drs. Douglas Lowy and Brajendra Tripathi, NIH) and wild-type and *CDK5* patient fibroblasts (gift from Dr. Daniella Magen, Ruth Rappaport Children's Hospital) were grown in AmnioMAX C-100 basal media supplemented with antibiotic-antimycotic (Life Technologies) and mycoplasma removal agent (Bio-Rad). U2-OS and HeLa cells were transfected using Lipofectamine RNAiMAX (Life Technologies) with 60pmol of STEALTH siRNA (Life Technologies) per six-well dish. Samples were analyzed 48 h post transfection. Plasmids were transfected using

Lipofectamine3000 (Life Technologies) according to manufacturer's recommendations. In brief, 2.5 μg of DNA and 5 μL of P3000 and Lipofectamine3000 were used per six well transfection. Cells were analyzed at the described time points. Cells were synchronized using a double thymidine (Sigma) block and release to capture cells at various cell cycle stages. To inhibit Dynein, U2-OS cells were treated with DMSO or 50 μM of Ciliobrevin in the dark for 1 hr at 37°C. CDK5 activity was inhibited using Roscovitine (Sigma) at a concentration of 20 μM overnight.

Centrosome enrichment

Asynchronous U2-OS cells were treated with 2 μM cytochalasin D and 1 μg/ml of nocodazole for 1.5 hr to depolymerize actin and microtubules, respectively. Centrosomes were enriched on a discontinuous sucrose gradient (70, 50 and 40% sucrose) and collected fractions were analyzed by western blotting.

Western blotting and immunoprecipitation

HeLa cells were incubated on ice with PBS (Life Technologies) for 5 min, harvested with a cell scraper (Corning) and lysed on ice in lysis buffer (1% IGEPAL630 (Sigma and Thermo Fisher), 50mM Tris pH7.4 (Life Technologies), 150mM NaCl (Ambion) in PBS) supplemented with protease and phosphatase inhibitor cocktail III (Sigma). For each immunoprecipitation 500μg of total lysate was incubated with 1-2 μg of antibody for 2 h and then incubated with magnetic protein G-Sepharose (GE Healthcare Life Sciences) for an additional 1.5 hours. Immunoprecipitating proteins were boiled in 2X Laemmli sample buffer with β-mercaptoethanol (Bio-Rad) or collected in pH2.0 Glycine (Life Technologies) and quenched in Tris pH9.0 (Ambion) for mass spectrometry analysis. Protein from flash frozen gestational week 23 brains were extracted using the NE-PER Kit (Thermo Fisher) followed by homogenization with a pellet pestle (Kimble). Reduced samples were separated on 4%–15% TGX gels (Bio-Rad), transferred to supported BA85 Protran (GE Healthcare) and subjected to immunoblot analysis using ECL lightening Plus (Perkin-Elmer) or LiCOR Odyssey scanner for quantitative analysis.

Mass spectrometry analysis

Immunoprecipitations from HeLa cell lysates were analyzed as previously described (Kodani et al., 2015). Immunocomplexes were digested with trypsin (Promega) peptides were then analyzed using a LTQ Oribtrap Velos Pro ion-trap mass spectrometer (Thermo Fisher). Captured peptide identity was determined using Sequest software (Thermo Fisher) and filtered for peptide false discovery.

Immunostaining

Adherent cells were grown on sterilized cover glasses (Azer Scientific) and fixed with chilled methanol for 3 min to visualize centrosomal proteins and 2 min for microtubules. Fixed cells were blocked in blocking buffer (2.5% BSA (Sigma), 0.1% Triton X-100 (Fisher) and 0.03% NaN_3 in PBS (Life Technologies). Primary, secondary antibodies, and Hoechst33342 (Life Technologies) were diluted in blocking buffer and incubated with cells for at least 1 h at room temperature. To detect CEP85L, cells were blocked in 2.5% FBS instead of BSA. To immunolabel CEP85L and α-tubulin in fetal brain samples, sections were permeabilized using 0.3% Triton X-100 in PBS, and incubated with antibody overnight in antibodies diluted in 300mM NaCl, 0.2% gelatin and 0.3% Triton X-100 (Paridaen et al., 2013). Stained samples were mounted using Gelvatol and imaged on an inverted Zeiss Axio Observer Z1, LSM700 or LSM800 with Airyscan microscope. Flash frozen sections from a gestational week 23 brain were fixed in 4% PFA overnight, permeabilized using 0.3% Triton X-100 in PBS and quenched in 0.1M glycine pH7.4. Sections were subsequently incubated with primary antibody in 0.3% Triton X-100, 300mM NaCl and 0.2% gelatin. Subsequently, the samples were mounted using Flouromount-G (Southern Biotech).

Migration assay

siRNA transfected U2-OS cells were grown to confluency on uncoated plastic bottom 6 well dishes. Monolayers were scratched using a P200 Rainin pipette, rinsed and imaged continuously using a Zeiss Celldiscoverer 7 for 24 hr. The Celldiscoverer chamber was set to 37°C with injected 5% CO_2. Compiled images and videos were processed using the ZEISS ZEN software. Cell migration was calculated using the MRI Wound Healing Tool macro in FIJI.

Microtubule regrowth assay

U2-OS cells transfected with SC or *CEP85L* siRNA were treated with 200nM Nocodazole (Sigma) for 1.5 hours. Cells were washed with cold media and placed on ice for 30 min. Warm media was added to the cells and allowed to recover at 37°C for the indicated time periods prior to fixation in cold methanol.

In utero electroporation of mouse embryos

pCDNA DEST53 CMV-GFP-U6 scrambled control or *Cep85l* shRNA and mCherry were electroporated into the ventricles of embryonic day 12.5 and 14.5 mice as previously described (Saito, 2006; Yang et al., 2012). In brief, plasmids (1 μg/ul) were injected into the telencephalic vesicle of embryos using a pulled micropipette. Five pulses of 30–50 V (950ms duration) were delivered across the embryo's head using a BTX ECM830 pulse generator. Electroporated embryos were collected and analyzed by immunohistochemistry. mCherry positive cells in each cortical layer were quantified using FIJI and compared using a Chi-square test.

QUANTIFICATION AND STATISTICAL ANALYSIS

To determine the statistical enrichment of mutations in CEP85L, we used the MedCalc's a Fisher exact probability calculator to determine statistical significance.

For the migration assay, the wounded area over the time course was analyzed using the MRI Wound Healing Tool macro in FIJI.

For all immunofluorescence quantifications intensities were quantified using the ROI tool in the FIJI software. The fluorescence of the control was set as 100% and used to calculate the fluorescence of the treatment and represented as a percentage of the control.

DATA AND CODE AVAILABILITY

Data from the mass spectrometry of CP110 and CEP85L immunoprecipitations are available as Table S3.